Characterisation of shallow sediments by processing of P, SH and SV wavefields in Kaštela (HR)

Federico Da Col [*], Flavio Accaino, Gualtiero Böhm, Fabio Meneghini

Istituto Nazionale di Oceanografia e di Geofisica Sperimentale – OGS, Borgo Grotta Gigante 42/c, 34010 Sgonico, Trieste, Italy

A B S T R A C T

A seismic study was conducted in a historical town in Croatia to characterize the shallow subsurface and evaluate the response to an earthquake for engineering purposes. The study involves three seismic lines acquired along the existing roads of the town. For each of the lines, we acquired vertical compressional P and two horizontally polarized, S-wavefields; SH and SV, respectively orthogonal and parallel to the direction of the seismic line. We processed the data from these three wavefields with both first-break tomography, to obtain wave-velocity profiles, and reflection seismic imaging, to obtain stacked sections, and integrated the results. From such analyses, we obtained an in-depth characterization of the shallow subsurface. Specifically, we obtained standard engineering parameters like the equivalent shear-wave velocity of the upper 30 m of the subsurface (V_{S30}), which indicates A-class soil, and compressional to shear-wave velocity ratio (V_P/V_S), which gives an indication regarding the presence of fractures in the rock. In addition to this, we evaluated the presence of anisotropy thanks to the SH- and SV-wave tomography inversions, which allowed to notice that $V_{SV} > V_{SH}$ on most of the area. The presence of anisotropy is consistent with the known geological features of the area, in particular the subvertical bedding of the flysch, of which we were able to estimate the bedding plane orientations (dip and strike angles). Finally, by superimposing the stacked sections obtained from reflection seismic imaging with the velocity profiles computed with the traveltime tomography, we confirmed the reliability of the tomographic velocity models.

1. Introduction

The evaluation of the seismic resistance of a building requires in-depth information about both the status of the building and the geotechnical parameters of the soil on which it is built. In fact, the stiffness of the soil determines its ability to amplify the incoming seismic waves. The soil parameters can be evaluated in a laboratory test (Lancellotta, 2008; Kramer, 1996) or in situ (e.g., Cone Penetration Test, Standard Penetration Test or Load Bearing Test). However, these methods provide one-point, non-areal information. For this reason, geotechnical sampling should be coupled with non-invasive geophysical surveys for the evaluation of the soil response to a natural macroseismic event (among others: Finn, 1991; Sitharam and Anbazhagan, 2008; Cardarelli et al., 2014). In particular, seismic surveys provide information regarding the seismic velocities in the shallow layers closest to the buildings, which can be used to estimate the strength of the medium and therefore its amplification level (Ansal et al., 2010). In fact, the seismic velocity itself is related to the elastic moduli of the medium and depends on the strain level; however, the relation is not linear (Vucetic, 1994). Following this, the most common engineering parameter to classify the strength of a medium is the equivalent horizontally polarized seismic shear-wave velocity of the first 30 m of subsoil (V_{S30}). This parameter is also part of the legislation regarding seismic engineering and was first accepted in the United States of America with the Uniform Building Code of 1977 (Dobry et al., 2000). Subsequently, it also entered the European legislation thanks to the Eurocode 8 provisions (Sabetta and Bommer, 2002).

Several seismic methods are used to compute the V_{S30}, both active and passive. Regarding the active seismic methods, a very common tool is the Multichannel Analysis of Surface Waves (Park et al., 1999; Socco and Strobbia, 2004), the reliability of which has been assessed by Comina et al. (2011). Another common tool is the first-break tomography of an SH seismogram (Motazedian et al., 2011; Chan et al., 2018). Also, high-resolution seismic reflection imaging can be used to evaluate the V_{S30}, provided the signal-to-noise ratio is high enough (Motazedian et al., 2011). Another reason why seismic reflection can also be a valuable tool is its ability to detect the presence of sharp contrasts in acoustic impedance, i.e., density, like in the case of contact between the topsoil and the bedrock, which can produce resonance in case of an earthquake. In addition, multi-channel seismic provides an accurate image of the subsoil geometry which is important to estimate the possible presence of elastic energy focus areas.

Passive seismic methods can also be used to compute the V_{S30}. The most common method is the horizontal to vertical spectral ratio (HVSR,

---

Fig. 1. a) Location of the town of Kaštela on the Dalmatian coast. b) Position of the seismic lines in the historical centre of Kaštela. Image taken from Google Earth of April 3rd 2020.

Nakamura, 1989; Bard, 1999), which requires single-station multi-component recordings. By computing the ratio between the vertical and horizontal spectra, the method allows to compute 1D vertical S-wave velocity models as well as the resonant frequency.

Even though the legislation regarding constructions is based on the V_{S30} parameter, a deeper knowledge of the shallow layers of the subsoil can be useful for engineering purposes. For example, an estimation of V_p/V_s (or Poisson's ratio) can be a proxy for the determination of porosity and elastic wave displacement (Lancellotta, 2008). Also, an indication of fluid saturation can be inferred from such ratio, since the S-wave velocity propagation is almost unaffected by the presence of fluids, while the P-wave is (Grelle and Guadagno, 2009; Uhlemann et al., 2016). Furthermore, an in-depth study of the subsurface can provide important information such as the depth of the weathered layer, from which builders can determine the depth of the foundations for heavy infrastructure (Agoha et al., 2015).

In this work, we present the results of the processing of three high resolution seismic lines acquired along the roads of a town on the Eastern Adriatic coast, where some important historical buildings are present. The aim of the study is to give the engineers an in-depth knowledge of the characteristics of the soil on which these buildings are constructed, in order to implement the best preservation interventions.

The dataset was acquired in an unconventional manner, as we generated and recorded vertical - compressional P- and two horizontally polarized - shear-wavefields, SH and SV, vibrating on a plane perpendicular to the direction of propagation, respectively orthogonal and parallel to the direction of the seismic lines. In fact, while acquisition and processing of P- and SH-waves is growing in popularity in the near-surface geophysics community (e.g., Cardarelli et al., 2014; Chen et al., 2017), very few examples can be found involving all three wavefields. On the other hand, seismologists interested in anisotropy performed several numerical studies (e.g., Leary et al., 1987; Fishman and Ahmad, 1995), but hardly any field data example of a controlled-source dataset like the one we show here is present in the literature.

Careful analysis of SH- and SV- wavefields to obtain their corresponding velocities was of particular importance, as a 24 channel geophone array aiming at surface wave analysis failed to provide clear dispersive events, making it therefore impossible to extract shear-wave velocities by performing a multichannel analysis of surface waves.

2. Geological setting

The town of Kaštela Kambelovac lies on the north shore of the Bay of Castles, between the cities of Split and Trogir, in Croatia. A map showing the location of the town is shown in Fig. 1. Overall, the bay is 15 km long and 5 km wide.

As for the tectonic point of view, the area is part of the Adriatic

structural unit (Herak, 1991) and is composed of clastic Eocene flysch and carbonate rocks. These rocks lie in a compressional system (Herak, 1986) striking NW-SE and were therefore subject to intense reverse faulting, folding and thrusting and the area can be identified as an "imbricate structure" (Buljan et al., 2006). More precisely, the main fault is the Kozjak reverse fault, in the northern part of the area, which caused the thrusting of older Upper Cretaceous sediments over younger Upper Cretaceous sediments as well as the thrusting of the entire Turonian/Senonian carbonate complex over the flysch (Marincic et al., 1973; Buljan et al., 2006).

Babic and Zupanic (2008) describe the origin of the Eocene flysch as corresponding to the underfilled stage of a foreland basin clastic succession which occurred contemporary to the Dinarides uplifting. Furthermore, they estimate its thickness to approximately 800 m to 900 m. The clastic flysch is mainly composed of layers of marls of variable thickness (from a few centimetres to 150 cm), with interlayers of calcirudites and calcarenites. Šestanović et al. (2012) identify the thinner bedding as corresponding to the parts of the flysch where the marls are interlayered with calcarenites, while a thicker bedding is observed where the marl is interlayered with calcirudites. Because of the tectonic context, the outcrops in the area show a sub-vertical bedding of the flysch and the presence of strong weathering.

Previous geotechnical investigations (Buljan et al., 2006; Šestanović et al., 2012) indicate that the flysch is characterized by low permeability, with permeability given mostly by the presence of layers of karstified calcirudites and/or calcarenites. The groundwater flows from East to West, as proved by the presence of freshwater springs in the Bay (Fritz and Bahun, 1997). Buljan et al. (2006) performed a refraction seismic experiment and estimate the thickness of the weathered layer in 1 m to 4 m, where the P-wave velocities range from 1000 to 1500 m/s. Velocities increase with depth, where less weathering occurred and exceed 4000 m/s at 8 m depth. These values match the findings of laboratory experiments performed by Šestanović et al. (2012).

3. Data acquisition

We acquired three lines along the roads of the town. A bird-eye view of the location of the three lines can be seen in Fig. 1. Lines 1 and 2 are 300 m long, while Line 3 is 160 m long. The sensors are geophones with a central frequency of 10 Hz, placed every 2 m in all three lines listening for two seconds with a sampling interval of 1 ms. The total number of active receivers during each shot for Lines 1 and 2 is 150, while for Line 3 is 81. To acquire the compressional waves, vertical geophones were used, while horizontal geophones were used while acquiring the shear-waves. The latter were re-oriented orthogonal and parallel to the direction of the seismic line when acquiring SH and SV wavefields respectively. Source points are every 4 m and we acquired two common shot gathers at each point. We used as a source two vibrators, mounted
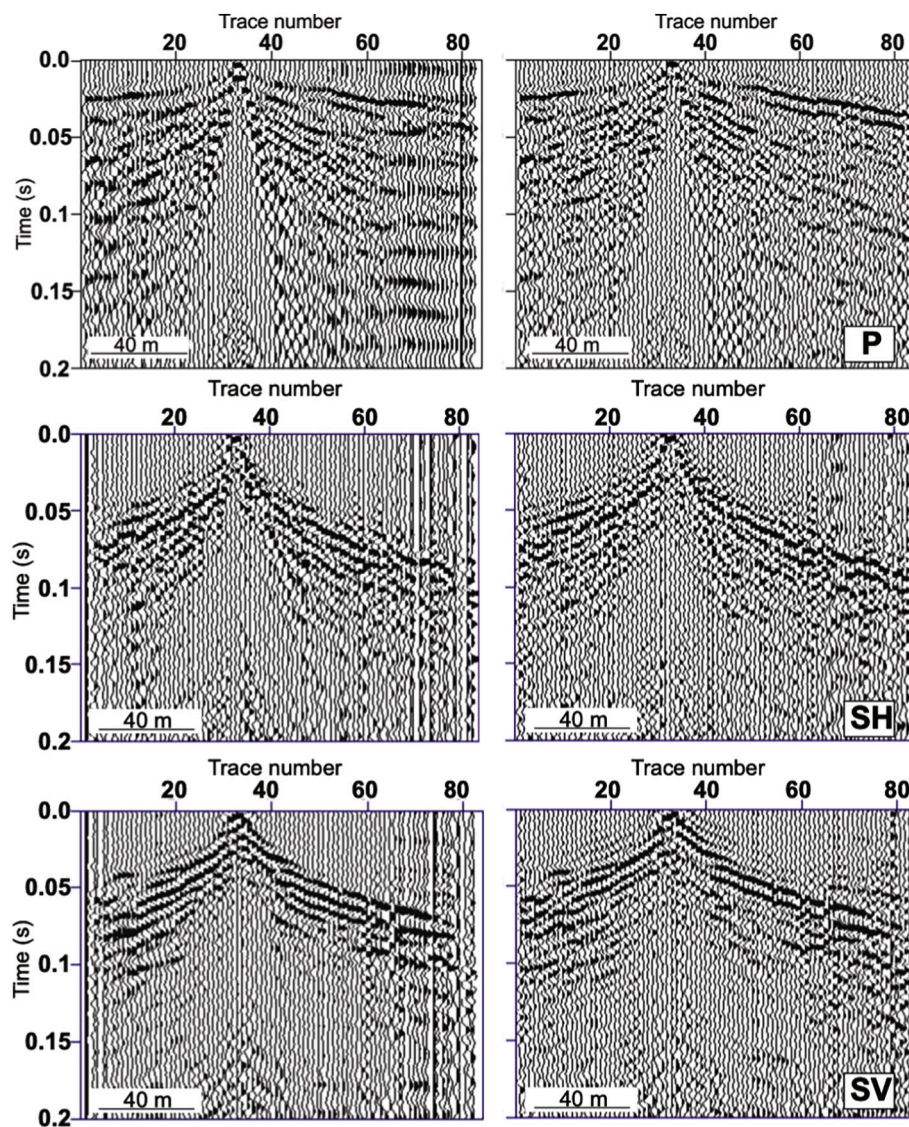
Fig. 2. Common shot gather relative to shot between stations 32 and 33 of Line3 before (left) and after application of pre-correlation predictive deconvolution to the data (right) Each seismogram is relative to the wavefield indicated in the label present in the bottom-right corner.

on a wheelbarrow, one producing P-waves, the other S-waves, re-orienting the latter parallel and orthogonal to the line to produce SV and SH waves respectively. For both P and S waves we used the same sweep ranging from 20 to 160 Hz, with a length of 15 s.

To be noted that during the acquisition of Lines 1 and 2 car traffic was intense in the town, while during the acquisition of Line 3 it was a lot quieter. Additional noise to Lines 1 and 2 was given by strong wind and some rain, while during the acquisition of Line 3 the weather was fine.

4. Methods

We processed the data both for seismic reflection imaging and for first-break tomography and then compared and integrated the results by overlaying the time-converted velocity profiles obtained by the tomography with the stacked sections obtained by reflection seismic imaging.

As for the pre-processing of the data, as a first step, we applied a predictive deconvolution before cross-correlating the recorded traces with the sweep signal, as in Baradello and Accaino (2013). This step significantly enhances the signal to noise ratio eliminating some of the coherent noise. As an example, we show (Fig. 2) the common shot

gathers (shot 33, Line 3) relative to all three acquired wavefields (P, SH and SV) without (left) and with (right) the application of the predictive deconvolution. Furthermore, after cross-correlation, we stacked in time domain the shot gathers repeated at the same shot point, in order to remove random noise and increase the coherent signal.

4.1. First-break tomography

We picked and inverted the first arrivals on each of the three acquired wavefields (P, SV and SH) for all the three lines. In the inversion, the picked travel-times were considered associated to diving waves ray paths. We used the Cat3D software (Böhm and OGS Research Group, 2014), which is based on minimum time ray tracing (Böhm et al., 1999) and uses the Simultaneous Iterative Reconstruction Technique (SIRT) as inversion algorithm (Stewart, 1993).

In the inversion procedure we applied the staggered grid method (Vesnaver and Böhm, 2000). First, we defined a starting grid with large pixels, characterized by a well-posed tomographic system (low null space). Then the grid was shifted several times in space (both X and Y directions), obtaining different grids, each used for computing separate inversions. All the tomographic results were then summed and averaged
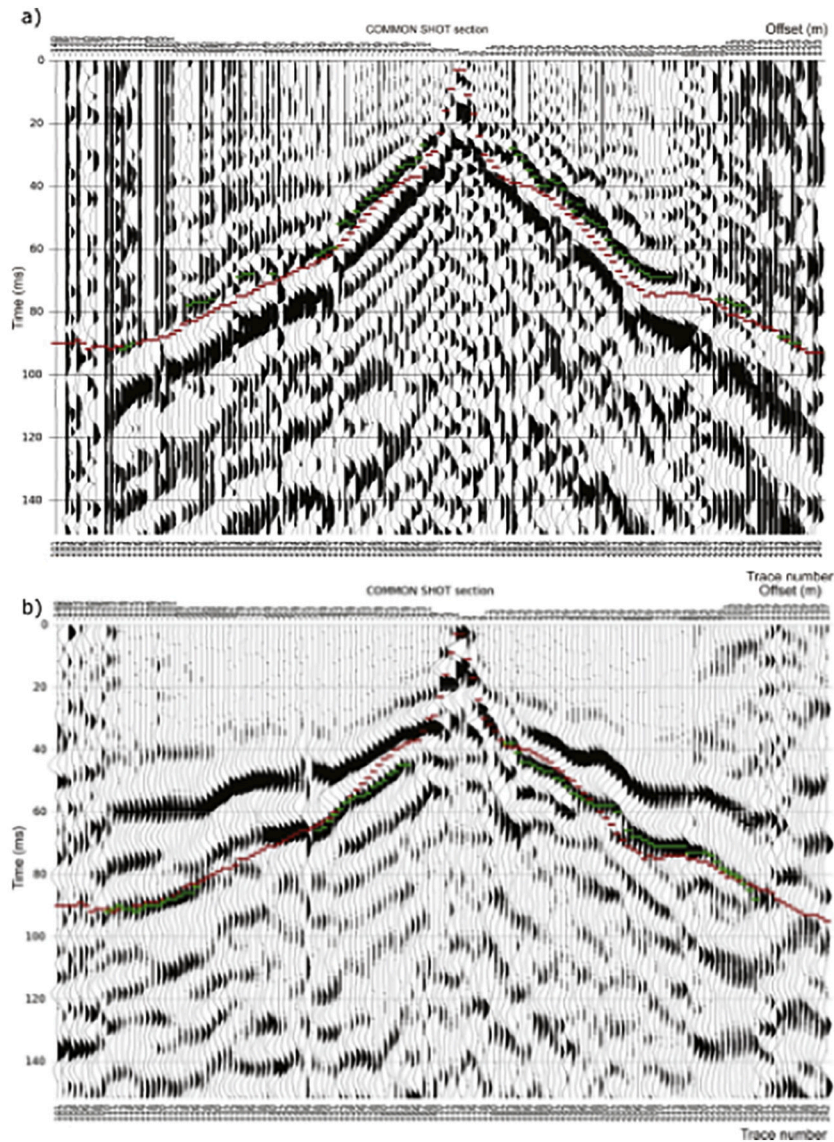
Fig. 3. Common shot gathers of shot 75 of Line1. a) SH-wavefield, b) SV-wavefield. In red we overlay the traveltimes we computed from the P-wave raytracing which we use as a guide for picking and in green the picked traveltimes. (For interpretation of the references to color in this figure legend, the reader is referred to the web version of this article.)
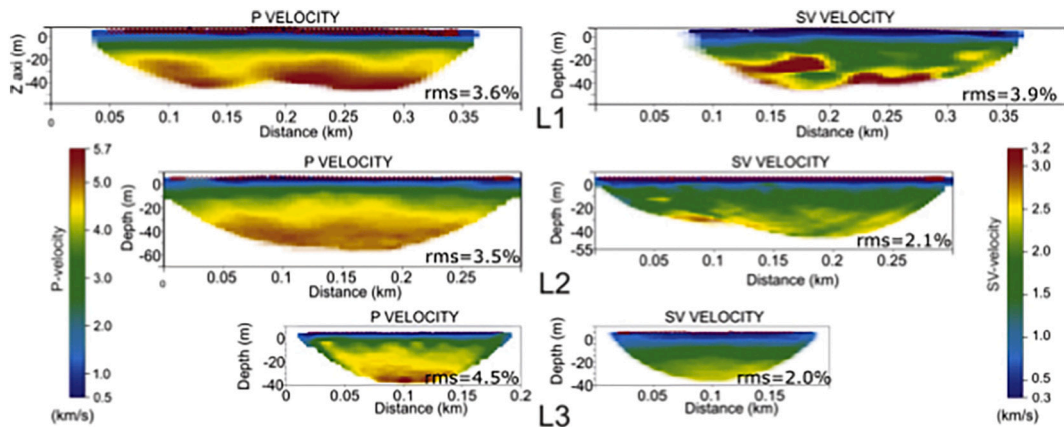

Fig. 4. Tomographic velocity sections of P (left) and SV (right) in the three acquired lines. For each velocity section, the average root mean square error is reported.
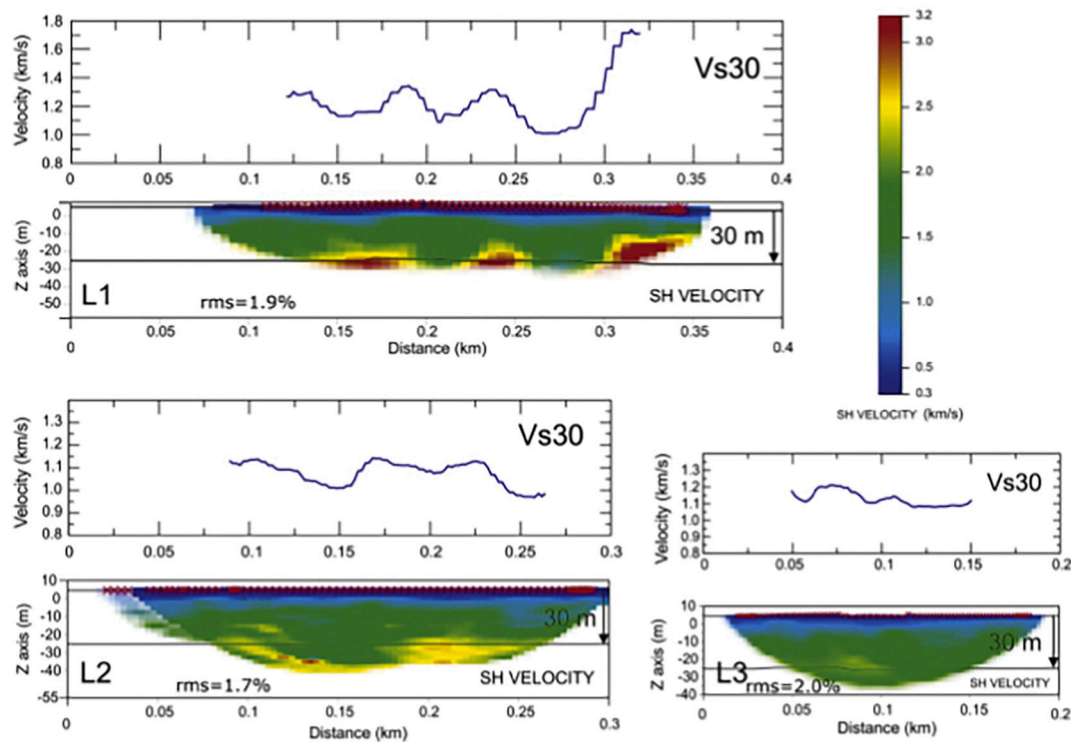
Fig. 5. Tomographic velocity sections of SH velocity in the three acquire profiles. V_{S30} along the profiles are also imaged. The mean rms error is reported below each velocity section.

on a single grid by oversampling the dimension of the original one, following the number of shifts applied to the starting grid. In this way, we obtained a final higher resolution grid without losing the property of the well-posed tomographic system present in the starting grid.

During the picking, the first arrivals on some of the common shot gathers relative to the S-waves were not as evident as those of the P-waves, creating an ambiguity on which phase to pick. To solve this issue, we computed travel-times by ray tracing on the P velocity model. Then, assuming $V_P/V_S = 1.73$, we displayed them on the S-wave common shot gather and used them as a guide to identify the correct S arrivals to pick. In Fig. 3 we show an example of common shot gathers from Line1 of the SH- and SV-wavefields, overlaying the computed first arrivals we used as a guide for picking.

Furthermore, V_{S30} values were computed from the travel-times obtained by vertical ray tracing from 30 m depth up to the topographic surface on the SH velocity tomographic model.

Fig. 4 shows the results of the P and SV first break tomographic inversions, while Fig. 5 shows the results of the SH first break tomographic inversion. V_{S30} values along the lines are also shown. The RMS errors at the last iteration are indicated next to each velocity profile.

In order to check the reliability of the traveltime inversion, two methods were used. First, we computed a null space map, which provides a measure of the reliability of the tomographic system (model discretization and ray distribution). It is based on the Singular Value Decomposition (SVD) of the tomographic matrix, which contains the ray segments belonging to each pixel of the model for all the considered rays. This analysis is applied to the starting grid used in the staggered grid method, in order to verify the correct choice of the model discretization. In all the inversions computed in this work (from P, SV and SH arrivals) we obtain a very low null space distribution in the starting grid for all the models considered. Fig. 6a) shows an example of null space map computed on the starting model used for the inversion of the L1 P data.

The second method considered is the time residual analysis, which provides a useful estimate of the error on the traveltimes. For each

inversion we considered the time residuals, that is, the difference between the picked and the computed traveltime for each source-receiver couple. We computed the distribution of these values with respect to all the considered records and the corresponding rms values (Fig. 6b). Furthermore, these residuals were also mapped onto a source vs receiver plot where the records affected by large errors (due to bad picking or error in source/receiver position) can be identified, eventually excluding the corresponding traveltimes from the records to be inverted. An example of residual map, computed on the inversion of P arrivals related to line L1, is shown in Fig. 6c, where the large time errors can be easily recognized.

4.2. Seismic reflection

The processing steps performed on the data are summarized in the workflow shown in Fig. 7.

After applying the geometries and correcting for the mild topography with the static corrections, we filtered the data with a bandpass having cutoff frequencies of 5–10–130-160 Hz. Furthermore, a notch filter with a central frequency of 50 Hz was applied to remove the noise from the powerlines. We then removed more noise by means of the trimmed mean dynamic dip filter (TMDDF) (Holcombe and Wojslaw, 1992). The algorithm is performed on pre-stack data and it aims at removing high amplitude random noise, as well as weak coherent noise, without eliminating useful trace information. At each sample of each trace the algorithm computes a series of trimmed means along rays (dips within a user-defined range of angles), using the sample itself and a user-defined number of leading and trailing traces. Trimmed mean operation means that a user-determined number of the smallest and largest samples along the dips are removed from the summation to reduce the effects of random noise. The output sample is the trimmed mean that yields the highest amplitude.

The stacking velocities were obtained from semblance analysis on supergathers formed by three common midpoint gathers. When correcting for normal move-out, we applied a stretch mute percentage of
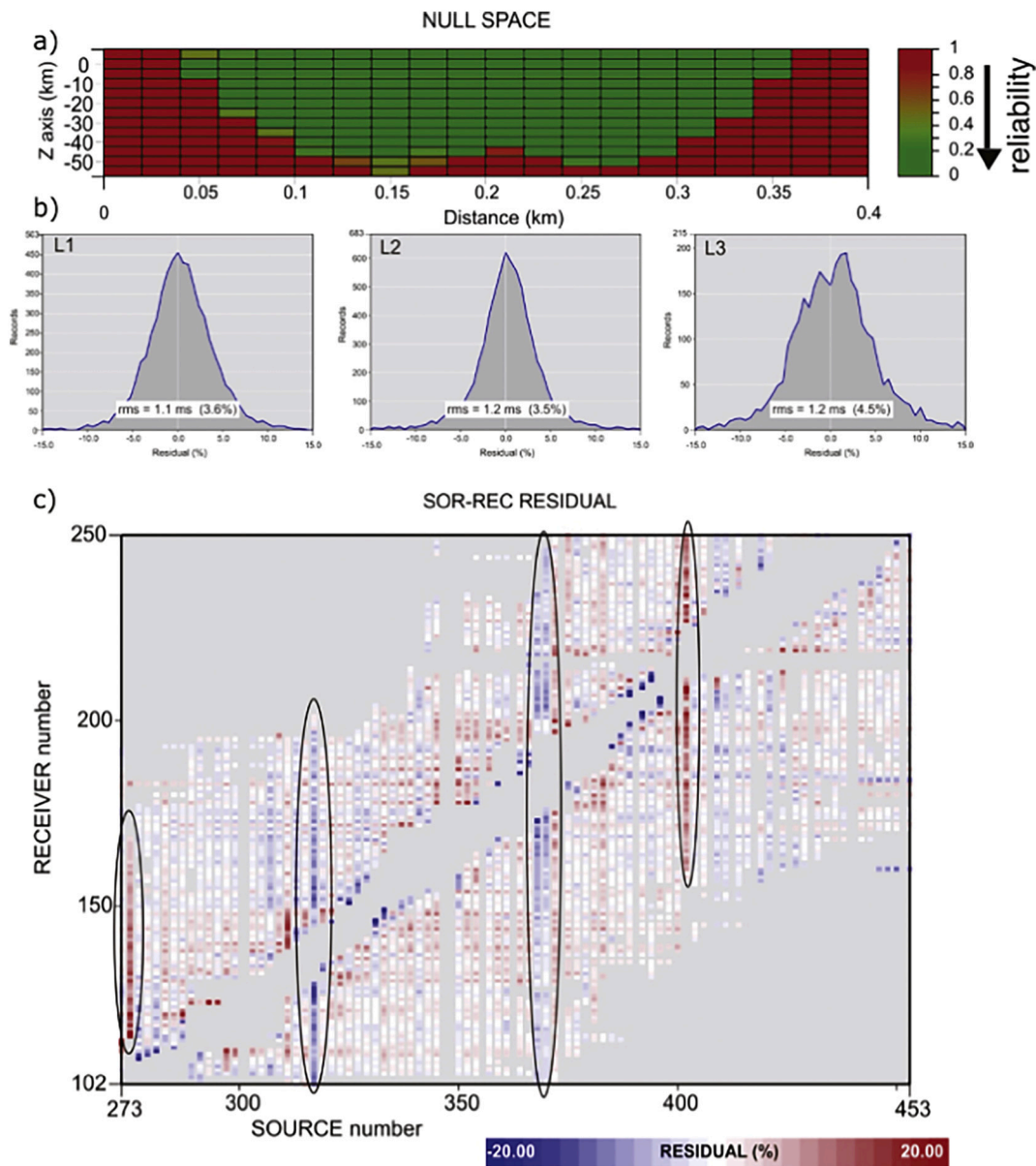
Fig. 6. a) Null space distribution on the starting grid used in the staggered grids procedure for the P traveltime inversion of line L1. The colorbar indicates the null space and therefore the reliability of the model from 1 (not reliabile) to 0 (very reliable). b) Time residual distribution of the P-wave traveltime inversion relative to all three lines. c) Time residual map related to the P-wave traveltime inversion of line L1. The black ellipses highlight the shots affected by large residual errors.

30%, but we also paid special attention to the large offstes, where we eliminated manually any stretched wavelet which could affect the results of the stacked section.

In order to validate the results of both tomographic and reflection seismic processing, we superimposed the stacked sections with the tomographic velocity profiles. To do this, the depth-domain velocity profiles were converted to time-domain using Seimic Unix software (Stockwell Jr, 1999). The results of such overlay are shown in Fig. 8 (Line 1) and 9 (Line 3).

Due to the presence of strong wind and rain, the stacked sections relative to Line 2 are too noisy and present no significant reflectors and are therefore not shown in this work. It is otherwise evident that the best results come from Line 3, where the signal to noise ratio is higher.

5. Results and discussion

In all the velocity profiles shown in Figs. 4 and 5, we observe the presence of a significantly lower velocity shallow layer, with P- and S-

wave velocities of approximately 800 and 600 m/s respectively. These values match those found in previous geotechnical investigations and correspond to weathered flysch (Šestanović et al., 2012; Buljan et al., 2006). The velocity then quickly increases with depth, reaching values of 3500 and 2500 m/s in the deepest part of the profiles, for P- and S-waves respectively. There is an overall increase in the velocities in the eastern lines (L2 and L3) compared to those in the western L1 line, both for the P and S sections.

The values of V_{S30} in all three lines exceed 800 m/s (see Fig. 5) and therefore allow us to categorize this as A-class soil.

In order to further investigate the properties of the rocks, we computed the V_P/V_{SH}, obtaining the plots shown in Fig. 10a). The ratio is high in all three lines, with significantly higher values in the eastern lines L2 and L3. We interpret this, together with the lower velocities, as due to the presence of stronger fracturing in the rocks. Furthermore, the very high values (>3) present in some areas of L2 and especially in L3 could be caused by the presence of fluids in the fractures. Fig. 11a) shows the cross-plots of the P-wave velocities versus the V_P/V_S, with
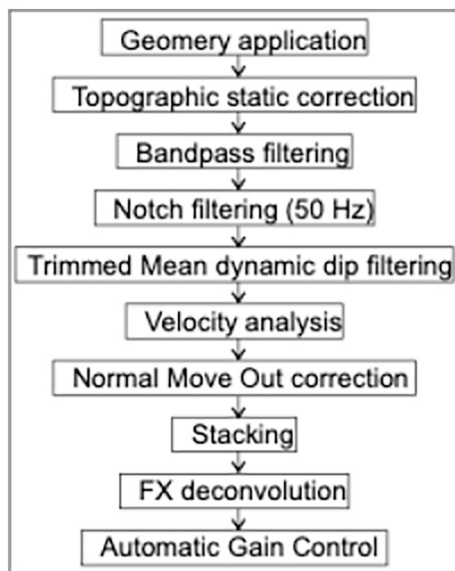
Fig. 7. Processing workflow relative to reflection seismic imaging.

respect to depth, indicated by the color of the dots. In the plot relative to Line1, there is an overall increase with depth of the V_P/V_S ratio, which probably indicates the presence of fluid-saturated fractures, while at intermediate depth a stiffer rock layer is present. As for Line 2 and Line 3, very high V_P/V_S ratios can be observed at shallow depth (> 3) indicating the presence of unconsolidated material (e.g. gravel below the road surface). In Line 2, similarly to Line 1, we observe at intermediate depths the presence of an area with lower V_P/V_S (~ 2.3), which is not present in Line 3. Line 2 also confirms the higher V_P/V_S ratio at larger depth observed in Line 1, while this cannot be confirmed in Line 3, due to the lower penetration depth reached by the tomography.

Furthermore, we observe that the SV velocity field (Fig. 4) differs from the SH velocity field (Fig. 5). So, we computed the V_{SH}/V_{SV} profiles, shown in Fig. 10b, and the cross-plots of SV velocities versus V_{SV}/V_{SH}, shown in Fig. 11b. Along all three profiles in Fig. 10b, the V_{SV}/V_{SH} is greater than 1 in most of the model. This indicates the presence of anisotropic effects in the investigated area, especially in Line 2 and Line 3, while in Line 1 the values of V_{SV}/V_{SH} are more scattered around 1. More specifically, at the same depths where low V_P/V_S is present, values of SV-velocities are slightly lower than those of SH further indicating the presence of less fractured rock.

The presence of anisotropy is consistent with the known sub-vertical bedding of the flysch and we provide an estimate of the possible orientation of the layering. In Eq. (1) the vertical and horizontal
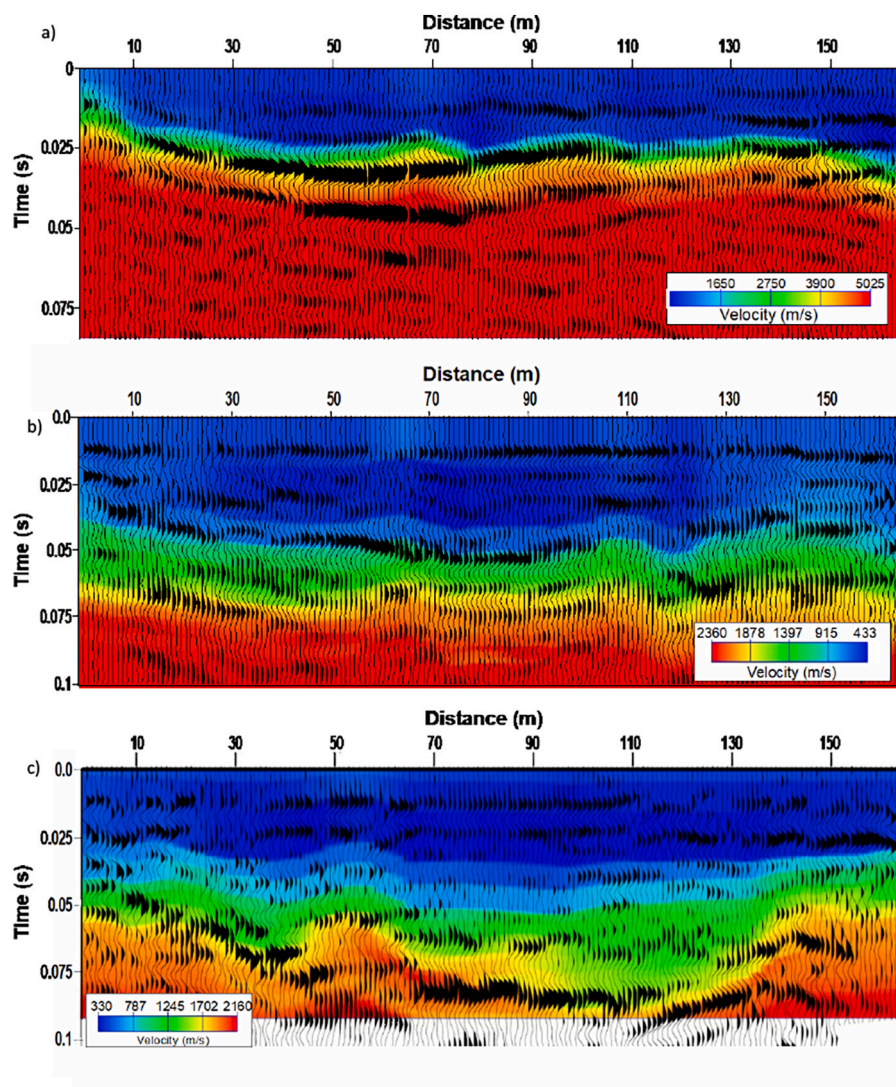

Fig. 8. Superimposition of the tomographic velocity profiles with the stacked sections of Line 1. (a) P-waves, (b) SH-waves, (c) SV-waves.
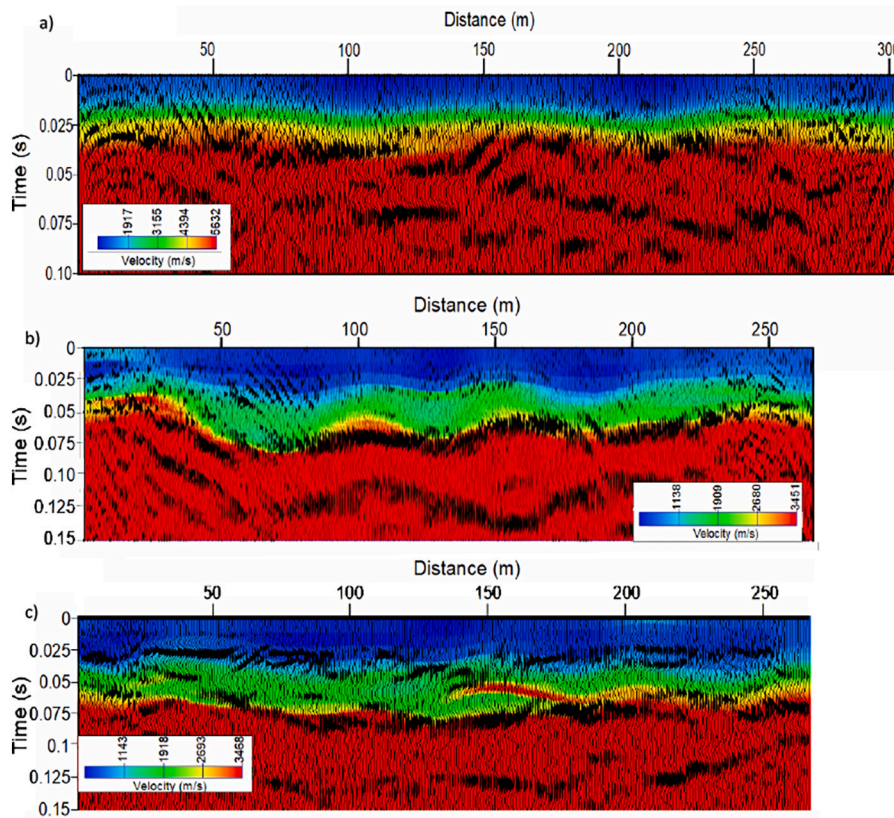
Fig. 9. Superimposition of the tomographic velocity profiles with the stacked sections of Line 3(a) P-waves, (b) SH-waves, (c) SV-waves.

components in case of non-vertical angle of incidence of the rays with the anisotropic plane (Thomsen, 1986; Böhm, 2020) are defined as:

$$V_{SV}(\theta) \approx V_{S_\perp} \left[1 + \left(\frac{V_{P_\perp}}{V_{S_\perp}} \right)^2 (\varepsilon - \delta) \sin^2\theta \cos^2\theta \right], V_{S_H}(\theta) \approx V_{S_\perp} \left[1 + \gamma \sin^2(\theta) \right]$$

(1)

where:

θ: angle of ray direction with axis of symmetry

$\gamma = \frac{V_{S_\parallel} - V_{S_\perp}}{V_{S_\perp}}$

ε, δ: Thomsen parameters

$V_{P_\perp}$: P velocity at vertical incidence ($\theta = 0$)

$V_{S_\parallel}$: S velocity parallel to the planes of anisotropy (maximum velocity component)

$V_{S_\perp}$: S velocity perpendicular to the planes of anisotropy (minimum velocity component)

In Fig. 12 we consider a situation where anisotropy is generated either by the presence of thin layers having different velocities (V1 is different to V2), or the layers present the same velocities (V1 is equal to V2), but the medium is fractured along the bedding direction. In these situations, let α be the angle of incidence of the ray with the anisotropic plane. Since we are considering diving ray paths, we can assume that the rays propagate in sub-horizontal direction in the deeper part of the
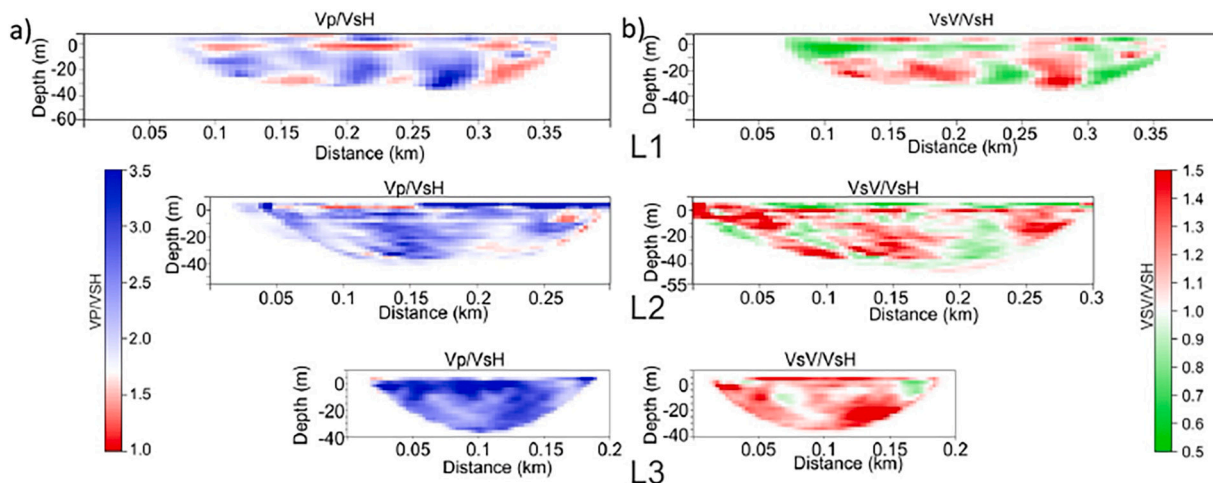

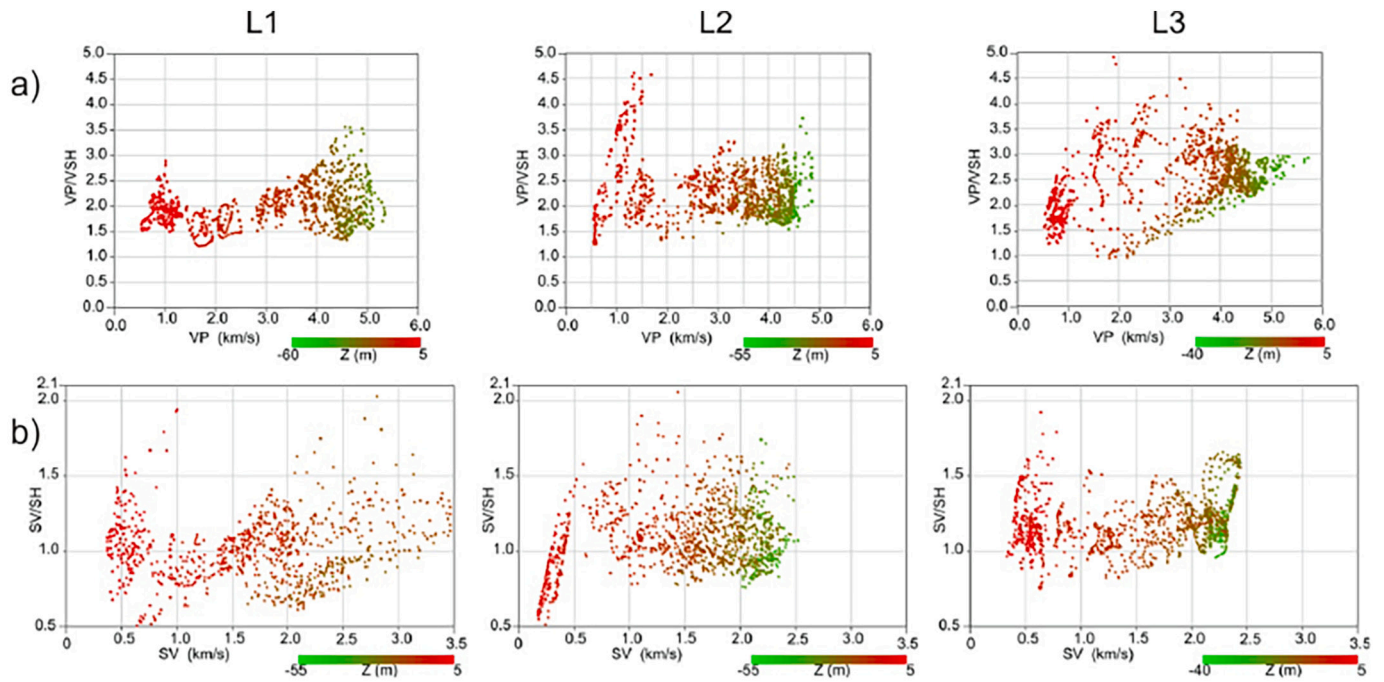**Fig. 10.** a)V_P - V_S ratios and b) V_{SH} -V_{SV} ratio for the three lines.

Fig. 11. Cross-plots a) V_P-V_S ratio versus P-wave velocity and b) V_{SV}-V_{SH} ratio for the three lines. The color of dots indicates the depth.
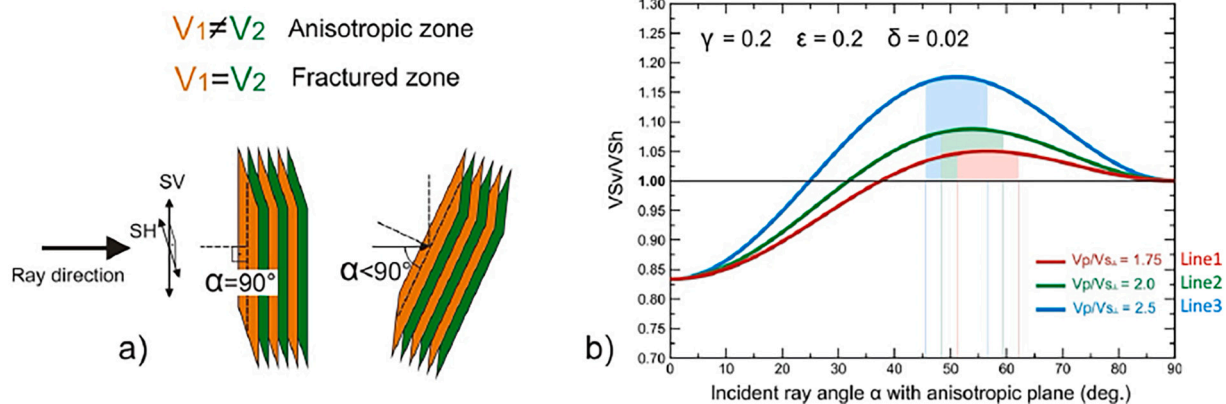

Fig. 12. a) Schematic representation of the vertical orientation of the anisotropic layers with respect to the horizontal ray direction. b) Graphic representation of the Vsv/VSh vs the incident ray angle with the anisotropic plane, obtained from Eq. (1), considering $\gamma = \varepsilon = 0.2$, $\delta = 0.02$ and related to different values of Vp/Vs. The Vp/Vs values correspond to the average values of the three lines.

tomographic model. Our data analysis showed that V_{SV}/V_{SH} is greater than 1 and we can estimate the Thomsen parameter ε of the flysch to be of about 0.2, as shown by Picotti et al. (2018) in a similar geological setting. We also assume similar anisotropic conditions for the S waves ($\gamma = \varepsilon$) and a weak value of the Thomsen parameter $\delta = 0.02$. Finally, if we consider the average value of V_p/V_s in each of the three lines and the angles of incidence corresponding to the highest values of V_{SV}/V_{SH} (Fig. 12b), we can estimate the dip angle (deviation from the horizontal plane) of the flysch to be between 45° and 60°.

Very similar considerations can be made for the strike angle (deviation from azimuth). However, in this case the components in Eq. (1) must be considered inverted. Therefore, the highest values of the V_{SV}/V_{SH} can be associated to angles of incidence with the anisotropic plane between 0° and 30°. These correspond to strike angles between 60° and 90°. Both strike and dip angles are consistent with the values shown in the geological map by Buljan et al. (2006).

By looking at the overlay of the tomographic velocity profiles with the stacked sections in Fig. 8, we notice that the position of the reflectors

matches quite well those of the main velocity transitions found by the tomography. For L1, P-wavefield, shown in Fig. 8 a), we see a very strong reflection corresponding to the main velocity transition (from green to red, in the plot).

From the stacked section relative to the S-wavefield (Fig. 8b,c) more reflectors can be detected with respect to the P-wavefield, thanks to the lower velocities of the S-waves and the consequent shorter wavelengths involved. This means that S profiles provide a better vertical resolution.

The best results are achieved from L3 (Fig. 9), where, due to the higher signal to noise ratio, we observe an excellent match between the velocity anomalies obtained by tomography and the reflectors detected by the stacked section. In particular, for the SV and SH wavefields, almost all of the velocity contrasts found in the tomography image have a corresponding reflector in the stacked section.

6. Conclusions

A seismic survey was performed, aiming at an in-depth

characterization of the shallow layers of the subsurface below a historical town on the eastern Adriatic coast. Given the complex geology of the area, composed of strongly fractured Eocene flysch, we decided to acquire a dataset which can be rarely found in the literature. The uncommonness of such dataset lies in the fact that the three high-resolution seismic lines were acquired using a setup able to record compressional as well as two horizontally polarized shear wavefields, one parallel to the seismic line, while the other orthogonal to it. We then evaluated the imaging capabilities of such data in terms of both first-break tomography and reflection seismic imaging.

The results show an overall decrease in velocity in the eastern lines (L2 and L3), when compared to the western line (L1). This, together with the increased V_P/V_{SH} indicates the presence of a more fractured medium and possibly the presence of fluids in the fractures. The values of the V_{S30} exceeding 800 m/s in all three lines allow us to identify the area as an A-class soil.

Furthermore, the acquisition of SH and SV wavefields allows us to detect the presence of anisotropy, which is consistent with the known geological features of the area. In fact, the sub-vertical bedding of the flysch can be identified as the cause of the larger SV than SH velocities. Finally, we are also able to give an estimate of the bedding plane orientations (dip and strike angles).

The results of the tomography are then overlayed with those of the stacked sections obtained from reflection seismic imaging. The positions of the reflectors match those of the changes in the velocity found by the tomography.

We can therefore conclude that the acquisition of compressional and shear waves, polarized in both directions with respect to the seismic line, in very complex media like the fractured and strongly deformed flysch present in the Bay is a valuable tool to characterize the shallow subsurface. Furthermore, this acquisition opened a question regarding the estimation of the anisotropic effects in such complex media which will be a topic of research for the coming years.

Declaration of Competing Interest

The authors declare that they have no known competing financial interests or personal relationships that could have appeared to influence the work reported in this paper.

References

Agoha, C.C., Opara, A.I., Okereke, C.N., Onwubuariri, C.N., Emberga, T.T., Inyang, G.E., Chilaka, J.C., 2015. Weathered layer determination and its effects on engineering structures: case study of parts of the Niger Delta. World 3 (2), 40–51.

Ansal, A., Kurtuluş, A., Tönük, G., 2010. Seismic microzonation and earthquake damage scenarios for urban areas. Soil Dyn. Earthq. Eng. 30 (11), 1319–1328.

Babic, L., Zupanic, J., 2008. Evolution of a river-fed foreland basin fill: the North Dalmatia flusch revisited (Eocene, outer dinarides). Nat. Croat. 17–4, 357–374.

Baradello, L., Accaino, F., 2013. Vibroseis deconvolution: a comparison of pre and post correlation vibroseis deconvolution data in real noisy data. J. Appl. Geophys. 92, 50–56.

Bard, P.Y., 1999. Microtremor measurements: a tool for site effect estimation? In: Irikura, K., Kudo, K., Okada, H., Sasatani, T. (Eds.), The Effects of Surface Geology on Seismic Motion. Balkema, Rotterdam, the Netherlands.

Böhm, G., 2020. Azimuthal Anisotropy in Layer Media from SV and SH Velocities Obtained by Ray-Based Tomography. In: 26th European Meeting of Environmental and Engineering Geophysics. Near Surface Geoscience. Virtual conference. 7–8 December 2020.

Böhm, G., OGS Research Group, 2014. Cat3D. Computer Aided Tomography for 3-D models. User Manual. OGS.

Böhm, G., Rossi, G., Vesnaver, A., 1999. Minimum-time ray tracing for 3-D irregular grids. J. Seism. Explor. 8, 117–131.

Buljan, R., Pollack, D., Pest, D., 2006. Engineering geological properties of the rock mass along the Kastela Bay sewage system. Geol. Soc. Lond. 740. IAEG2006.

Cardarelli, E., Cercato, M., De Donno, G., 2014. Characterization of an earth-filled dam through the combined use of electrical resistivity tomography, P-and SH-wave seismic tomography and surface wave data. J. Appl. Geophys. 106, 87–95.

Chan, J.H., Catchings, R.D., Goldman, M.R., Criley, C.J., 2018. VS30 at Three Strong-motion Recording Stations in Napa and Napa County, California—Main Street in Downtown Napa, Napa Fire Station Number 3, and Kreuzer Lane—Calculations Determined From s-wave Refraction Tomography and Multichannel Analysis of Surface Waves (Rayleigh and Love), 2018-1161. US Geological Survey.

Chen, J., Zelt, C.A., Jaiswal, P., 2017. Detecting a known near-surface target through application of frequency-dependent traveltime tomography and full-waveform inversion to P- and SH-wave seismic refraction data. Geophysics 82 (1), R1–R17.

Comina, C., Foti, S., Boiero, D., Socco, L.V., 2011. Reliability of V_{S30} evaluation from surface-wave tests. J. Geotech. Geoenviron. 137 (6), 579–586.

Dobry, R., Borcherdt, R.D., Crouse, C.B., Idriss, I.M., Joyner, W.B., Martin, G.R., Seed, R. B., 2000. New site coefficients and site classification system used in recent building seismic code provisions. Earthquake Spectra 16 (1), 41–67.

Finn, W.D.L., 1991. Geotechnical engineering aspects of microzonation. In: Proc. 4th International Conf, Vol. 1, pp. 199–259.

Fishman, K.L., Ahmad, S., 1995. Seismic response for alluvial valleys subjected to SH, P and SV waves. Soil Dyn. Earthq. Eng. 14 (4), 249–258.

Fritz, F., Bahun, S., 1997. The morphogenesis of submarine springs in the Bay of Kastela, Croatia. Geol. Croat. 50/1, 105–110.

Grelle, G., Guadagno, F.M., 2009. Seismic refraction methodology for groundwater level determination:"Water seismic index". J. Appl. Geophys. 68 (3), 301–320.

Herak, M., 1986. A new concept of geotectonics of the Dinarides. Prirodosl. istraz. 51. Acta Geol. 16/1, 1–42. Zagreb.

Herak, M., 1991. Dinarides – mobilistic view of the genesis and structures. Acta Geol. 21/ 2 (Zagreb).

Holcombe, H.T., Wojslaw, R.S., 1992. Spatially weighted trim stacking: a technique for pre-stack noise suppression. In: Proceedings, Society of Exploration Geophysicists, 1992 Annual Meeting, pp. 1157–1160.

Kramer, S.L., 1996. Geotechnical Earthquake Engineering. Prentice Hall, Upper Saddle River, NJ.

Lancellotta, R., 2008. Geotechnical Engineering. CRC Press.

Leary, P.C., Li, Y.G., Aki, K., 1987. Observation and modelling of fault-zone fracture seismic anisotropy—I. P, SV and SH travel times. Geophys. J. Int. 91 (2), 461–484.

Marincic, S., Magas, N., Borovic, I., 1973. Osnovna geoloska karta SFRJ 1:100.000, List Split i pripadaju i tumac Karte, K 33-21 (Basic Geological map of Republic of Croatia, the Split Area and Pertaining Key to the Map, K 33-21). Institute of Geology, Zagreb (in Croatian).

Motazedian, D., Hunter, J.A., Pugin, A., Crow, H., 2011. Development of a VS30 (NEHRP) map for the city of Ottawa, Ontario, Canada. Can. Geotech. J. 48 (3), 458–472.

Nakamura, Y., 1989. A method for dynamic characteristics estimation of subsurface using microtremor on the ground surface. Railway Tech. Res. Inst. (Q. Rep.) 30 (1), 2530.

Park, C.B., Miller, R.D., Xia, J., 1999. Multichannel analysis of surface waves. Geophysics 64 (3), 800–808.

Picotti, S., Dal, Cin M., Böhm, G., Busetti, M., 2018. Evidences of seismic flysch anisotropy in the Gulf of Trieste. In: 24th European Meeting of Environmental and Engineering Geophysics. Near Surface Geoscience 2018, 9–13 September, Porto, Portugal.

Sabetta, F., Bommer, J., 2002. Modification of the spectral shapes and subsoil conditions in Eurocode 8. In: 12th European Conference on Earthquake Engineering (paper ref. 518).

Šestanović, S., Toševski, A., Mihalić, S., Dečman, A., Ferić, P., 2012. Preliminary data for development of the engineering geological map of the city of Split (Croatia). Environ. Earth Sci. 66 (5), 1547–1556.

Sitharam, T.G., Anbazhagan, P., 2008. Seismic microzonation: principles, practices and experiments. EJGE Spec. Vol. Bouquet 8, 61.

Socco, L.V., Strobbia, C., 2004. Surface-wave method for near-surface characterization: a tutorial. Near Surf. Geophys. 2 (4), 165–185.

Stewart, R., 1993. Exploration seismic tomography: fundamentals. In: Domenico, S.N. (Ed.), Course Note Series, vol. 3. SEG - Society of Exploration Geophysicists.

Stockwell Jr., J.W., 1999. The CWP/SU: seismic Un* x package. Comput. Geosci. 25 (4), 415–419.

Thomsen, L., 1986. Weak elastic anisotropy. Geophysics 51 (10), 1954–1966.

Uhlemann, S., Hagedorn, S., Dashwood, B., Maurer, H., Gunn, D., Dijkstra, T., Chambers, J., 2016. Landslide characterization using P- and S-wave seismic

refraction tomography — the importance of elastic moduli. J. Appl. Geophys. 134, 64–76.

Vesnaver, A., Böhm, G., 2000. Staggered or adapted grids for seismic tomography? Lead. Edge 19 (9), 944–950.

Vucetic, M., 1994. Cyclic threshold shear strains in soils. J. Geotech. Eng. 120 (12), 2208–2228.